Au/TiO 2 (P25)-gC 3 N 4 composites with low gC 3 N 4 content enhance TiO 2 sensitization for remarkable H 2 production from water under visible-light irradiation

Pablo Jiménez-Calvo, Valérie Caps, Mohamed Nawfal Ghazzal, Christophe Colbeau-Justin, Valérie Keller

Nano Energy 75 (2020) 104888

Contents lists available at ScienceDirect

Nano Energy

journal homepage: http://www.elsevier.com/locate/nanoen

Au/TiO_2(P25)-gC_3N_4 composites with low gC_3N_4 content enhance TiO_2 sensitization for remarkable H_2 production from water under visible-light irradiation

Pablo Jiménez-Calvo [a,1,*], Valérie Caps [a], Mohamed Nawfal Ghazzal [b], Christophe Colbeau-Justin [b], Valérie Keller [a,**]

[a] Institut de Chimie et Procédés pour l'Energie, l'Environnement et la Santé (ICPEES), UMR-7515 CNRS/Université de Strasbourg/ECPM, 25 rue Becquerel, 67087, Strasbourg, France
[b] Institut de Chimie Physique (ICP), UMR-8000 CNRS/Université Paris-Saclay, Bâtiment 349, 91405, Orsay, France

ARTICLE INFO

Keywords:
Au/TiO_2(P25)-gC_3N_4
Mass H_2 production rate
Z-scheme heterojunction
Photosensitization
Schottky junction

ABSTRACT

A series of ternary Au/TiO_2(P25)-gC_3N_4 heterostructure photocatalysts with low Au nanoparticle (NP) loading and gC_3N_4 content were synthesized and evaluated for H_2 production from water with a very low amount of sacrificial agent (1 vol%) under solar and visible-light irradiation. The optimized composite, 0.3 wt% Au/TiO_2(P25)-gC_3N_4 (95–5), exhibited a remarkable production rate under visible light (419 μmol^{-1} h^{-1} $g_{catalyst}$ of H_2), corresponding to almost twice the cumulated H_2 production over 2.5 h as that of the Au/TiO_2 (P25) reference. To best of our knowledge, this high of a yield has never been reported for comparable experimental conditions. The highest performing composite was characterized using UV–vis, XPS, UPS, BET, TEM, and TRMC techniques. The performance of the photocatalyst could be correlated to contributions of various phenomena such as effective heterojunction formation of TiO_2 with gC_3N_4 operating in a Z-scheme dynamic allowing TiO_2 photosensitization towards visible-light, also leading to new electronic hybrid states, and plasmonic Au/support Schottky junction allowing electronic trapping sites and co-catalytic effects. These contributions resulted in more efficient light harvesting and separation of the charge carriers to enhance visible light driven activity.

1. Introduction

Energy transition from fossil to renewable fuels needs further development to meet required global changes [1]. Among the renewable energies, solar energy is a promising substitute for fossil fuels because it uses one of the most powerful natural sources of energy: the sun [2]. The direct energy irradiated to the Earth from the Sun is on the order of 3.8×10^{24} J/year, and 0.04% capture is sufficient to supply global energy demands [3]. More efficient and direct conversion processes of sunlight into chemicals (solar fuels) that can be ideally stored for long time to supply electricity to the grid smartly are urgently needed [3,4]. Photocatalysis was discovered in 1972, when Fujishima and Honda showed the feasibility of using light, water, and a catalyst in a photoelectrocatalytic cell for artificial water splitting [5]. It is a promising technology for using sunlight to split water and obtain hydrogen (H_2), an influential energy vector for the foreseen low-carbon circular economy due to its high mass energy content (142 MJ/mol) compared to conventional fossil fuels such as methane (56 MJ/mol) [6].

Rational design and engineering of photocatalytic hybrid systems such as multi-phase heterostructures-based materials has been highly active in achieving high H_2 production during the last decade. This strategy aims at overcoming the limitations of individual semiconductors (SCs) by exploiting intimate and suitable contact of electronic and chemical interfaces [7], while simultaneously enhancing charge formation/separation and light harvesting. Heterostructures-based materials such as heterojunctions, plasmonics, and multi-phase composites have achieved important milestones and provided fundamental insights into H_2 production. However, in spite of these successes, the suitable photon-conversion to rich chemicals still represents a major challenge in the development of high-performing

* Corresponding author.
** Corresponding author.
E-mail addresses: pablo.jimenez-calvo@universite-paris-saclay.fr (P. Jiménez-Calvo), vkeller@unistra.fr (V. Keller).
[1] Current address: Laboratoire Physique des Solides, UMR-8502 CNRS/Université Paris-Saclay, 91405 Orsay, France.

https://doi.org/10.1016/j.nanoen.2020.104888
Received 23 December 2019; Received in revised form 20 March 2020; Accepted 24 April 2020
Available online 22 May 2020

visible-light photocatalysts.

In this context, heterostructures combining oxides, carbon-based and metallic nanoparticle (NP) systems aiming at forming staggered heterojunctions and Schottky junctions [8] have been reported to tackle this issue. One can briefly mention a few recent examples: g-C_3N_4/TiO_2 [9], A-TiO_2/Au/g-C_3N_4 [10], Au/TiO_2–CeO_2 [11], Cu_xO-TiO_2 [12], gC_3N_4/Au/$BiVO_4$ [13], TiO_2–WO_3–Au [14], Pt/WO_3–TiO_2 [15], CdS/TiO_2/WO_3 [16], and Pt–TiO_2/g–C_3N_4–MnO_x [17]. Most of the mentioned ternary and particularly the quaternary composite present efficient photogenerated paths that serve as reference systems. Thus, diverse innovative multi-component composites have progressed the field of semiconductor and plasmonic photocatalysis. Nevertheless, further research must be carried out to meet the ideal photocatalytic hybrid system, *i.e.*, a visible-light active SC, suitable conduction and valence band positions, high efficiency of absorption of photons and generation of charge carriers, and good stability over time.

Herein, a series of ternary Au/TiO_2(P25)-gC_3N_4 composites with low gC_3N_4 content were evaluated for photocatalytic H_2 production. This strategy is relatively fast, simple, and cost-effective, and it consists in a straightforward three-step synthetic protocol (wet impregnation, thermal polycondensation, and deposition of Au NP). The core of this investigation was to identify the optimal TiO_2(P25)-gC_3N_4 proportion at which the material enhances the charge carriers lifetime and improves light absorption, both functions resulting from exploiting the best intimate interface contact operating in an effective Z-scheme dynamic. Thus, Au/TiO_2(P25)-gC_3N_4 (95–5) resulted in the highest performing composite under both solar and visible light and TiO_2(P25)-gC_3N_4 (95–5) revealed unprecedented TiO_2 photosensitization effect at 360, 450, and even at 500 nm, as supported by TRMC results. To the best of our knowledge, this high H_2 yield (photoactivity) in the visible light and enhanced TiO_2 photosensitization (kinetics of free electrons) have never been reported for comparable experimental conditions. These new evidences and insights may serve as reference to rationally design improved visible-light heterostructure composites.

2. Experimental section

2.1. Materials

Melamine ($C_3H_6N_6$, 99%, Sigma Aldrich), dicyandiamide ($C_2H_4N_4$, 99%, Sigma Aldrich), AEROXIDE® titanium dioxide P25(TiO_2, 99%, Evonik Industries), chloroauric acid ($HAu^{III}Cl_4$) (≥99.9% trace metals basis, Alfa Aesar), sodium borohydride (≥98%, Sigma Aldrich), methanol (CH_3OH, ≥99.6%, Sigma Aldrich), ethanol (CH_3CH_2OH, ≥96%, Sigma Aldrich), and triethanolamine (TEOA, ≥99%, Sigma Aldrich), were used without further purification.

2.2. Synthesis

2.2.1. Synthesis of the references

Reference graphitic carbon nitride (gC_3N_4) was synthesized via thermal polycondensation of an equimolar ratio of melamine (1.92 g) and dicyandiamide (1.28 g) as described in the literature, with the difference that the synthesis was carried out under continuous flow atmospheric conditions [18]. The precursors were put into an alumina crucible with a lid. Thermal polycondensation was carried out in a tubular furnace applying a heating ramp of 5 °C min^{-1} until reach 550 °C and keeping it constant for 3 h in a continuous air flow of 100 mL min^{-1}.

Reference TiO_2 P25 (Evonik) was used without further treatment and it was referred as Bare TiO_2 and was also thermally treated at same experimental conditions as for gC_3N_4 thermal polycondensation. This treated material, different reference, was referred to as TiO_2 550C.

2.2.2. Synthesis of the nanocomposites

TiO_2(P25)-gC_3N_4, referred as TiO_2-gC_3N_4 for simplicity, nanocomposites were synthesized via two successive steps as described elsewhere [18]. In the first step, equimolar amounts of melamine and dicyandiamide blend were dissolved in 10 mL of distilled water and stirred in the presence of suspended TiO_2(P25). The solution was then evaporated at room temperature under vigorous stirring and the obtained powder was dried in an oven at 100 °C overnight. In the second solid state polycondensation step, the pre-impregnated TiO_2 was placed in an alumina crucible with a lid at 550 °C for 3 h (ramp of 5 °C min^{-1}) to obtain the final TiO_2-gC_3N_4 composite. Nanocomposites with a final gC_3N_4 content ranging from 2.5 to 10 (±0.5) wt% were synthesized. Only the highest gC_3N_4 content *i.e.,* 10 wt% was determined via thermal gravimetric analysis (Fig. S1 a-b), while the lower contents were determined using a theoretical approximation following a simple mathematical model that predicted the final mass proportion of TiO_2 and gC_3N_4 (see **S1**). The gC_3N_4 content was then calculated in equation (1):

$$gC_3N_4\ (wt\%) = \frac{m_{C_3N_4}}{m_{C_3N_4} + m_{TiO_2}} \quad (1)$$

For comparison, a physical mixture containing the same mass proportion of TiO_2 and gC_3N_4 (95–5) as the synthesized composite was prepared and then loaded with 0.3 wt% of Au. It was referred as Au/TiO_2-gC_3N_4 (95–5) mix.

2.2.3. Gold deposition

Au/support samples were prepared by chemical reduction of $HAuCl_4$ [19]. The support (300 mg) was dispersed in a methanol/ethanol mixture (91/9 v/v, 55 mL) with a tip sonicator (700 W, 20 kHz) for 30 min, using 30% of the maximum sonication power. The mixture was then transferred to a bath sonicator (280 W, 50/60Hz) and cooled to room temperature (22 °C) with the sonication off. A given volume of a methanol/ethanol solution of $HAuCl_4$ ($2.5(\pm0.2) \times 10^{-3}$ mol L^{-1}) was then added in order to target a gold loading of 0.3 wt%. Sonication was carried out for 1 h, whereupon 5 mL of a fresh methanol/ethanol solution of $NaBH_4$ (2.5×10^{-2} mol L^{-1}) was added. Sonication was then continued for 10 min. Finally, the powders were recovered by filtration and dried in the air at 110 °C in an oven for 12 h.

2.3. Materials characterization

UV–vis absorption spectra were recorded on a PerkinElmer Lambda 950 Scan spectrophotometer equipped with a 100 mm diffuse reflectance integrating sphere. For clarity of the results, diffuse reflectance (Rd) spectra were converted to Kubelka-Munk units according to $F(R) = (1 - Rd)^2/2Rd$, where $Rd = R_{sample}/R_{BaSO4}$ ($BaSO_4$ as the standard) [20]. To obtain the apparent band gap (Eg) of the SCs, the Tauc equation $(F(R) * h\nu)^s = h\nu - Eg$ was used, where h is the Planck constant, ν the frequency, and s a coefficient depending on the direct or indirect nature of the band gap transition (½ for gC_3N_4 and TiO_2) [21].

Nitrogen adsorption-desorption isotherms were obtained using a Micromeritics Asap 2420 porosimeter at 77 K using N_2 as an adsorbent. Materials were outgassed at 250 °C under a primary vacuum for 2h in order to desorb impurities from their surfaces and eliminate any water. Specific surface areas were calculated by the BET method in the relative pressure (p/p0) range of 0.05–0.3 and by using t-plots methods [22]. Pore-size distributions were calculated by the BJH method, specific for mesoporous solids.

Thermal Gravimetric Analysis was performed using a Q500IR instrument (TA Instrument). Each sample was placed in a platinum crucible and heated from room temperature up to 900 °C with a heating rate of 10 °C min^{-1} under an air flow of 25 mL min^{-1}. The standard deviation of the decomposition temperature of the as-prepared samples was ±10 °C.

XRD measurements were carried out on a Bruker D8-Advance diffractometer equipped with a Lynx Eye detector and operating at 40 kV and 40 mA in a θ-θ mode using the Kα radiation of Cu at 1.5418 Å.

The datasets were acquired in step scan mode over the 2θ range 10–60, using a step interval of 0.0329° and a counting time of 4 s per step. Samples were deposited on a round-shape glass plate. The mean crystallite size of TiO_2 anatase (101) and rutile (110) were determined using the Debye-Scherrer equation based on the full width at half maximum at 2θ = 25.2° and 27.5°, respectively.

Elemental analyses of the composites were performed using inductively coupled plasma atomic emission spectroscopy (ICP-AES). The limit of detection of the instrument was 0.1 mg L^{-1} for Au. Analysis of the gold component of the Au/support composite allowed the calculation of deposition yields which are defined as the ratio between the actual deposited mass of Au (deduced from ICP-AES analysis) and the mass of Au introduced during the deposition step (Table 1).

XPS measurements were performed in an ultrahigh vacuum (UHV) Thermo-VG scientific spectrometer equipped with a CLAM4 (MCD) hemispherical electron analyzer. The Al Kα line (1486.6 eV) of a dual anode X-ray source was used as the incident radiation. Survey and high-resolution spectra were recorded in the constant pass energy mode at 100 and 20 eV, respectively. The energy shift due to electrostatic charging was subtracted using the carbon adventitious signal, *i.e.*, the C 1s peak located at 284.6 eV. Surface atomic ratios were derived from XPS spectra using a Shirley-type background with the appropriate experimental sensitivity factors of the normalized photo ionization cross-section of the atomic subshells as determined by Scofield [23].

UPS measurements were performed in an ultrahigh vacuum (UHV) Thermo-VG scientific spectrometer equipped with a CLAM4 (MCD) hemispherical electron analyzer. During the UPS measurement (hν = 21.2 eV), a bias of 15.32 V was applied to the sample to avoid interference of the spectrometer threshold in the UV photoelectron spectra. The VBM values were determined by fitting a straight line on the leading edge and taking into account the $E_{cut\text{-}off}$.

High-resolution transmission electron microscopy (HRTEM) was performed on a JEOL 2100F LaB6 TEM/STEM microscope operating at 200 kV and with a point-to-point resolution of 0.21 nm and an X-ray microanalysis silicon drift detector. The sample was sonicated in ethanol before a drop of the suspension was deposited onto a microscopic copper TEM grid covered with carbon film for observation. ImageJ 1.43 software was used for statistical determination of the size of the gold nanoparticles and for determination of relative distances (dhkl) by electronic diffraction (ED) pattern analysis. The data analysis procedure was based on the measurement of the distance from the center of the image to the respective circle points.

TRMC analyses were performed using a Gunn diode of the K_α band at 30 GHz. The pulsed light source was an OPO laser (EKSPLA, NT342B) tunable from 225 to 2000 nm. The frequency of the pulse laser was every 8 ns fwhm at 10 Hz. The corresponding light energy densities received by the sample were 1.5, 10.8, 8.1, and 6.1 mJ cm^{-2} at 360, 450, 500, and 550 nm, respectively.

2.4. Photocatalytic tests

The photocatalytic activities of the Au/support composites were evaluated for H_2 production from water containing a very low amount of triethanolamine (TEOA) as a sacrificial agent (1 vol%) in a photocatalytic set-up as described elsewhere [24]. H_2 production was carried out in a quartz vessel containing 1 L of Milli-Q deionized water and equipped with a jacket quartz tube containing a 150 W Ceramic-Metal-Halide Hg Lamp, to simulate artificial solar light (21.1 mW cm^{-2}, Fig. S2). Visible-light simulated irradiation was achieved by adding a 0.1 g L^{-1} Nigrosing solution into the cooling solution flowing in the plunging quartz tube to cut off the UV photons, resulting in irradiance of 2.8 mW cm^{-2}, Fig. S2 [24]. The jacket was linked to a 20 °C water cooling bath to continuously cool the reaction to avoid any increase in water temperature that may occur as a result of heat from the light source. Prior to any experiment, residual oxygen was removed by nitrogen flushing. The photocatalytic tests were performed by suspending 250 mg of catalyst in *ca.* 0.1 mol L^{-1} TEOA aqueous solution under continuous nitrogen flow at 100 mL min^{-1} and with mechanical stirring at 700 rpm. The reaction products were analyzed online every 100 s by a μgas chromatography analyzer (R-3000, SRA Instruments) equipped with a thermal conductivity detector.

Stability and recycling ability were evaluated using photocatalytic test performed 2.5 h after reaching the plateau of H_2 production. After each photocatalytic test, photocatalyst was filtered, washed and dried. The photocatalyst was then re-used as previously described in the photocatalytic reactor. It should be noted that after each washing cycle there was a 5% mass loss. Stable H_2 production was considered to be the value after reaching a stable plateau. The hydrogen formation rate (r_{H2}) was defined as the evolution of H_2 over time (dn dt^{-1}), and was calculated according to equation (2), where Q_{N2} is the nitrogen flux and $V_{m\,H2,\ 20\ °C}$ is the molar volume of H_2 at 20 °C.

$$r_{H_2} = \frac{dn}{dt} = \frac{ppm_v * Q_{N_2}}{V_{m_{H_2,\ 20°C}}} \quad (2)$$

The accurate expression for H_2 evolution is often expressed in terms of mass hydrogen rate production ($r_{(m)H2}$), which is the r_{H2} divided by the mass of catalyst (m_{cat}) according to equation (3):

$$r_{(m)_{H2}} = \frac{r_{H_2}}{m_{cat}} = \frac{ppm_v * Q_{N_2}}{m_{cat} * V_{m_{H_2,\ 20°C}}} \quad (3)$$

IQY values were determined by measuring the absorbance of the photocatalyst suspension at the same concentration (0.25 g L^{-1}) as in the photocatalytic reactor. These absorbances were measured at the entrance and exit port of the integrating sphere, in order to measure the absorbance of the sample while minimizing the contribution of diffusion from catalyst particles. To determine the photon flux, the absolute irradiance of the lamp was measured using an ILT900-R spectroradiometer (International Light Technologies). IQY was calculated using equation (4), where $r_{(m)H_2}$ is defined as the hydrogen formation rate (mol h^{-1}) and $q_{p\ (Abs)}$ is defined as the photon flux absorbed by the photocatalytic material.

$$IQY = 2 \times \frac{r_{(m)_{H2}}}{q_{p\ (Abs)}} \quad (4)$$

$q_{p\ (Abs)}$ could be calculated according to equation (5), where P(λ), E(λ), and A(λ) are defined as the irradiation power, photon energy, and absorbance of the nanoparticle suspension, respectively, at a given wavelength (λ), of each sample used in the photochemical reactor, which has an optical path l = 5 cm.

Table 1
Physico-chemical properties of the as-prepared and reference samples.[a]

Sample	Deposition Yield‡ (%)	Au content (wt%)	Band gap† (eV)	S_{BET}* ($m^2\ g^{-1}$)	V_{pore} ($cm^3\ g^{-1}$)	Pore size** (nm)	Anatase‡ (101) (nm)	Rutile‡ (110) (nm)
TiO_2 550C	72 ± 4	0.22 ± 0.01	3.15 ± 0.05	46 ± 5	0.31 ± 0.02	39 ± 4	20 ± 1	27 ± 1
97.5–2.5	68 ± 4	0.20 ± 0.01	3.02 ± 0.05	50 ± 5	1.80 ± 0.06	48 ± 5	24 ± 1	26 ± 1
95–5	84 ± 5	0.25 ± 0.01	3.00 ± 0.05	47 ± 5	1.00 ± 0.04	33 ± 3	21 ± 1	27 ± 1
90–10	76 ± 4	0.23 ± 0.01	3.10 ± 0.05	52 ± 5	0.87 ± 0.04	33 ± 3	21 ± 1	27 ± 1
gC_3N_4	82 ± 4	0.25 ± 0.01	2.70 ± 0.05	10 ± 1	0.05 ± 0.02	42 ± 4	–	–

[a] ‡ = from ICP-AES; † = from Tauc plot; * = calculated using BET method; ** = calculated using BJH method; ‡ = mean crystallite size.

$$q_{p(Abs)} = \int_{\lambda_{min}}^{\lambda_{max}} \frac{P(\lambda) \times (1 - 10^{A(\lambda)l})}{E(\lambda)} \, d(\lambda) \quad (5)$$

3. Results and discussion

Nanocomposites were synthesized with a final gC_3N_4 content ranging from 2.5 to 10 (±0.5) wt% to be compared with their associated physico-chemical properties and activities.

3.1. UV–vis absorption properties

Fig. 1a exhibits the color of the TiO_2-gC_3N_4 composites and references, including their associated band gap values. The three ternary composites, 97.5–2.5, 95–5, and 90–10, are white, as it is TiO_2 550C reference, whereas the gC_3N_4 is yellow, which indicates a predominance of TiO_2 over gC_3N_4 in the ternary composites.

The UV–vis spectra via the Kubelka-Munk function (Fig. 1b) show that all composites exhibit a maximum absorption in the UV/blue range of the spectra (band edge at 386 nm) which is characteristic of TiO_2, although the absorption edge is slightly red-shifted. A second contribution with a maximum located at *ca.* 550 nm is attributed to the SPR (surface plasmon resonance) of the Au NPs. Fig. 1b (inset), shows that the SPR absorption is pronounced for all composites and for Au/TiO_2 550C reference but not for Au/gC_3N_4. Two reasons can be mentioned for the no clear visibility of the SPR signal in Au/gC_3N_4 reference. One is the modification in the dielectric constant of the Au NP environment and the other one is the distribution of Au NPs over non-porous gC_3N_4, and thus the density of Au NPs over C_3N_4, which is much more homogeneous and uniform throughout the sample than that observed over TiO_2-containing supports. The gC_3N_4 and TiO_2 550C references have the lowest (2.70 eV) and largest (3.15 eV) apparent band-gap values, respectively, as deduced by Tauc equation (Fig. 1c) [21]. The band gaps of the three composites are in between the values of the two references, but are closer to TiO_2, which supports the UV/vis spectral red-shifted.

3.2. BET surface area and BJH porosity

From Brunauer, Emmett, and Teller (BET) measurements (Table 1, Fig. S3a), it can be observed that all composites and references exhibit a type-IV adsorption-desorption isotherm profile, which is consistent with mesoporous materials [22,25,26]. The gC_3N_4 reference presents a S_{BET} value *ca.* 5 times lower than the other four samples. Whilst the surface area in TiO_2-based composites corresponds to external porosity, *i.e.* inter-crystallites porosity. It is thus related to the TiO_2 crystallite size (which controls the outer surface of TiO_2 crystallites) [27]. Then, S_{BET} is similar in all TiO_2-based composites (48 ± 3 m^2/g), because the crystallite sizes are similar (22 ± 2 nm and 26 ± 1 for anatase and rutile, respectively). The gC_3N_4 component does not contribute to the surface area, due to its low surface (10 m^2/g) and low content (<10 wt%).

The Barret-Joyner-Halenda (BJH) pore-size distributions (Table 1, Fig. S3b) exhibit a monomodal type for all samples. TiO_2(P25) 550C exhibited the largest pores, with a pore size centered at *ca.* 53 nm. The other five samples show smaller pores from 35 to 42 nm. However, comparing the pore volume values of the composite samples shows a different tendency. It can be seen that there is an increase in pore volume with decreasing gC_3N_4 content in the TiO_2-gC_3N_4 (90–10) (95−5) (97.5–2.5) composite series, representing 6, 3.3, and 2.9 times higher values than the TiO_2 550C reference, respectively and 36, 20, and 17 times higher pore volume than the gC_3N_4 reference, respectively. There is a significant difference between the pore volume of the composites compared with the two references, indicating that the pore volume increased when adding TiO_2 into the gC_3N_4 synthesis to obtain a composite with low gC_3N_4 content. This resulting porosity (0.87–1.80 cm^3/g) is much higher than the sum of those of the separate components (0.3 and 0.05 cm^3/g for TiO_2 and gC_3N_4, respectively). This is due to an efficient mixing of the two components at the nanoscale, which allows directing the synthesis of gC_3N_4 towards a much more porous material (analog to hard template) with deeper pore channels, while TiO_2 crystallites and surface of gC_3N_4 layers remain unchanged.

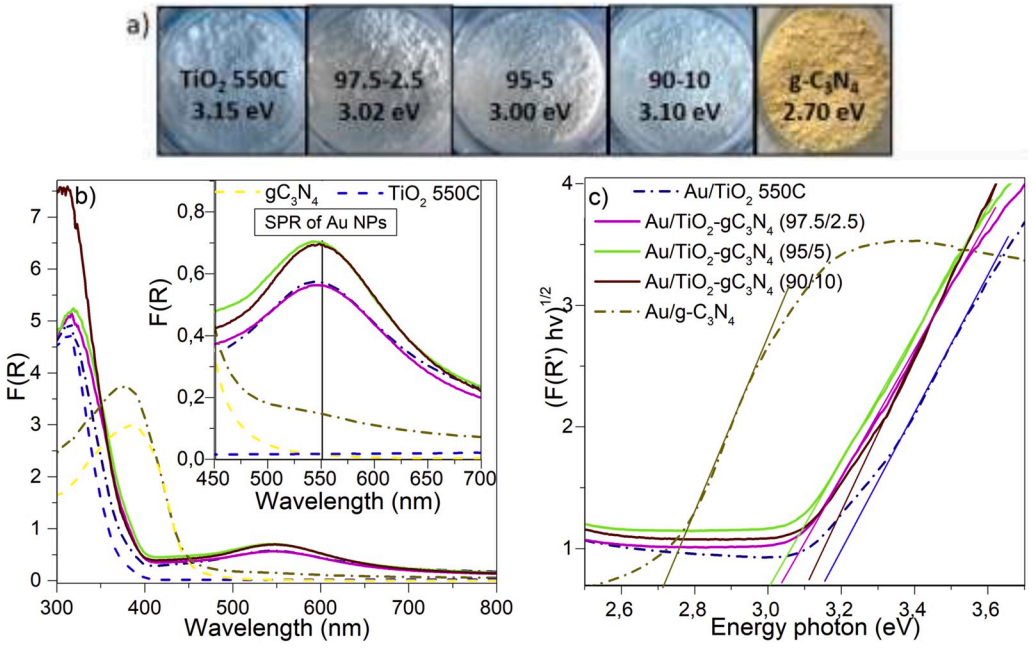

Fig. 1. a) Color of the three TiO_2-gC_3N_4 composites and reference powders b) UV–vis spectra of the 0.3 wt% Au/TiO_2-gC_3N_4 series of the composites and references with Au NPs. Magnification of the spectral domain corresponding to the SPR signal of Au NPs at approximately 550 nm (inset) c) Tauc plot to determine the apparent band gap of the samples.

3.3. Structural characterization, X-ray diffraction (XRD)

The XRD patterns (Fig. S4a) of the composites exhibit the main characteristic diffraction peaks at $2\theta = 25.2^{\circ}$ which corresponds to the anatase phase of TiO_2, indexed as the (101) diffraction plane. The diffraction peak observed between 27° and 28° (Fig. S4b) with its width and corresponding mean crystallite size, was assigned to the TiO_2 rutile phase indexed as the (110) diffraction plane rather than to the interlayer stacking of the π-conjugated aromatic systems of gC_3N_4 (indexed as the (002) plane). For TiO_2-gC_3N_4 composites exhibiting gC_3N_4 content lower than 10 wt%, XRD analysis could not provide evidence of gC_3N_4 because the crystallographic structure of TiO_2 is predominant. The mean crystallite sizes of TiO_2 domains were determined using the Debye-Scherrer relationship (Table 1), and it can be seen that there are no significant differences in crystallite size for any of the two phases (anatase and rutile) of the composites in comparison to the TiO_2 reference.

3.4. Elemental analysis

The Au deposition yield (Table 1) was 70–80% for all samples (composites and references). It should be noted that the Au deposition yield is higher for the gC_3N_4-containing samples than for TiO_2 550C. The small differences in the deposition yield leading to only small variations in the Au content ensure the photocatalytic H_2 production at the same Au content can be fairly compared [28].

3.5. X-ray photoelectron spectroscopy (XPS)

The survey spectra in Fig. S5a, show the contributions of O 1s, Ti 2p, N 1s, C 1s, and Au 4f at binding energies of *ca.* 530, 460, 400, 285, and 85 eV, respectively, for almost all the samples. The major contributions are N 1s and C1s for the Au/gC_3N_4 reference, and Ti 2p and O 1s for the TiO_2-based samples. Minor contributions are O 1s for Au/gC_3N_4 and C 1s for the TiO_2-based samples. For comparison, the corresponding mechanical/physical mixture (Au/TiO_2-gC_3N_4 (95–5) mix) was also added.

The Ti 2p signal in the two TiO_2-based samples, Au/TiO_2 550C and Au/TiO_2-gC_3N_4 (95–5) displays two major contributions at 463.9 and 458.1 eV, ascribed to Ti $2p_{1/2}$ and Ti $2p_{3/2}$, respectively, which are characteristic for Ti^{4+} in TiO_2 (Fig. 2a). The Au/TiO_2-gC_3N_4 (95–5) composite did not present any significant shift (higher than 0.5 eV) compared to the Au/TiO_2 550C reference but a shift is clearly present. The origin of this binding energy shift will be discussed in more detail in the following N 1s section. However, when comparing the Au/TiO_2 550C composite with the physical mixture (Au/TiO_2-gC_3N_4 (95–5) mix), a significant binding energy shift of *ca.* 1.4 eV is observed for the two Ti^{4+} peaks. Due to the mechanical sample nature, involving a separated diphasic heterostructures [29], it can be concluded that no additional bond is present, whatsoever. Nevertheless, a possible charge-induced effect [30] cannot be discarded.

The C 1s signal in the Au/TiO_2-gC_3N_4 (95–5) composite (Fig. 2b) shows three contributions at 288.4, 286.3, and 284.6 eV, which are ascribed to C═O, C–O or C–N═C, and C–C, respectively. These species can be attributed to carbonyl-carboxylate groups, sp^2-bonded C of N═C-$(N)_2$ from the heterocyclic ring [31] (coming only from the gC_3N_4 skeleton structure) or O–Ti–O–C–N interactions [32] (indicating the interaction between TiO_2 and gC_3N_4, that may confirm heterojunction formation), and to sp^2 adventitious carbon, which could come from defects of the graphitic domains. It can be seen that the Au/TiO_2 550C and Au/gC_3N_4 references display only two contributions, but with different attributes. The major contribution for Au/gC_3N_4 (287.4 eV) is assigned to sp^2-bonded C of N═C-$(N)_2$ from the heterocyclic ring and the minor contribution (284.6 eV) is assigned to the adventitious carbon. The major contribution for Au/TiO_2 550C (284.6 eV) is attributed to the adventitious carbon, and the minor contribution (288.4 eV) can be attributed either to C═O from carbonyl groups or to O_2 adsorbed species. Like the Au/TiO_2 550C reference sample, the Au/TiO_2-gC_3N_4 (95–5) physical mixture seems to present only two contributions, but with a different ratio between the contributions and with the minor contribution shifted toward a lower binding energy, probably due to others types of C–O bonds.

The N 1s signal in the Au/gC_3N_4 reference (Fig. 2c) exhibits two characteristic contributions, a major one at 399.9 and a minor one at 397.9 eV, which are assigned to the sp^2-hybridized pyridine nitrogen of C═N–C in the heterocyclic ring and to the N-$(C)_3$ tertiary nitrogen, respectively [33–35]. Whereof N 1s signal in the composite and mechanical mixture samples, in contrast to gC_3N_4 reference, presents only one broad peak with relatively low intensity (due to the low gC_3N_4 content) making deconvolution more difficult. Despite the low intensity, the deconvolution in both samples exhibit two peaks but with inverse proportions compared to the two typical gC_3N_4 reference signals. This proportion change may indicate that independently of the composite and mechanical mixture the abundancy of the pyridine and tertiary nitrogen-based species have changed. Interestingly, for the case of Au/TiO_2-gC_3N_4 (95–5) composite the signals of the tertiary nitrogen have shifted towards higher binding energy indicating a lower electron density, which simultaneously suggests an induced charge transfer already mentioned and found for the Ti 2p signal shift on the opposite direction (higher electron density). This modification of the chemical environment of N that may be correlated to two possible scenarios. The formation of O–Ti–O–C–N interactions [32], as deduced from the C 1s spectra or additionally to the presence of lone pairs of electrons of N can serve as a strong field inducing force pairing electrons (unhybridized p orbitals) with Ti d orbitals. Literature mentioned that oxides containing electron-acceptor centers are able to form a coordination bond with nitrogen containing molecules, TiO_2 and gC_3N_4 in our case, due to the excess of electron density by the nitrogen atoms with non-shared pairs of electrons. Ti^{n+} ions with orbital vacancies can be considered as strong adsorption centers on TiO_2 that can be filled with the free pair of electrons of the pyridine nitrogen, therefore donor-acceptor bond is thus possible [36]. On the other hand, N 1s signals of the physical mixture shift towards lower binding energy, as found for Ti 2p signals previously and confirms the charge transfer described.

Regarding the C/N ratio results, the reference gC_3N_4 exhibited 0.75, exactly as the predicted value for a perfect gC_3N_4 sheet, indicating that the gC_3N_4 structure is highly polymerized. Whilst, the C/N value was lower for the Au/TiO_2-gC_3N_4 (95–5) composite (0.52) compared with that of the reference Au/gC_3N_4 (0.75), possibly a result of the low mass gC_3N_4 content leading to the formation of a more linearly polymerized gC_3N_4 structure. Moreover, Au/TiO_2-gC_3N_4 (95–5) physical mixture exhibited a C/N ratio of 0.66, which is closer to the theoretical value than that of the composite, and which is in good agreement with the fact that proportions of Au/gC_3N_4 and Au/TiO_2 550C references were just physically mixed instead of formed into a composite.

The O 1s signals in the Au/TiO_2 550C reference (Fig. 2d) display three characteristic contributions at 533.2, 531.3, and 529.3 eV ascribed to adsorbed H_2O or O^{2-} species, hydroxyl surface groups (-OH), and Ti–O (major peak), respectively. Au/gC_3N_4 only presents the –OH contribution, but in a lesser relative amount than the TiO_2-based materials. However, the poorly hydroxylated surface of the gC_3N_4 support appears not to have limited Au NP deposition. Only two contributions were found shifted to lower binding energies with respect to Au/TiO_2 550C for the Au/TiO_2-gC_3N_4 (95–5) composite and physical mixture. Despite of the presence of an equivalent shift for the two samples, they may have different physical meanings. In the case of the composite, a charge transfer was hypothetically proposed in the N 1s discussion section, while this time the possible coordination interaction of the pyridine nitrogen is with oxygen species. OH-groups, even adsorbed water molecules can work as other acceptor-donor centers. Considering that hydroxyl groups have the ease to form H-bond that can also serve for the physical adsorption of molecules (polar molecules such as N containing molecules), which are considered acceptor of protons [36].

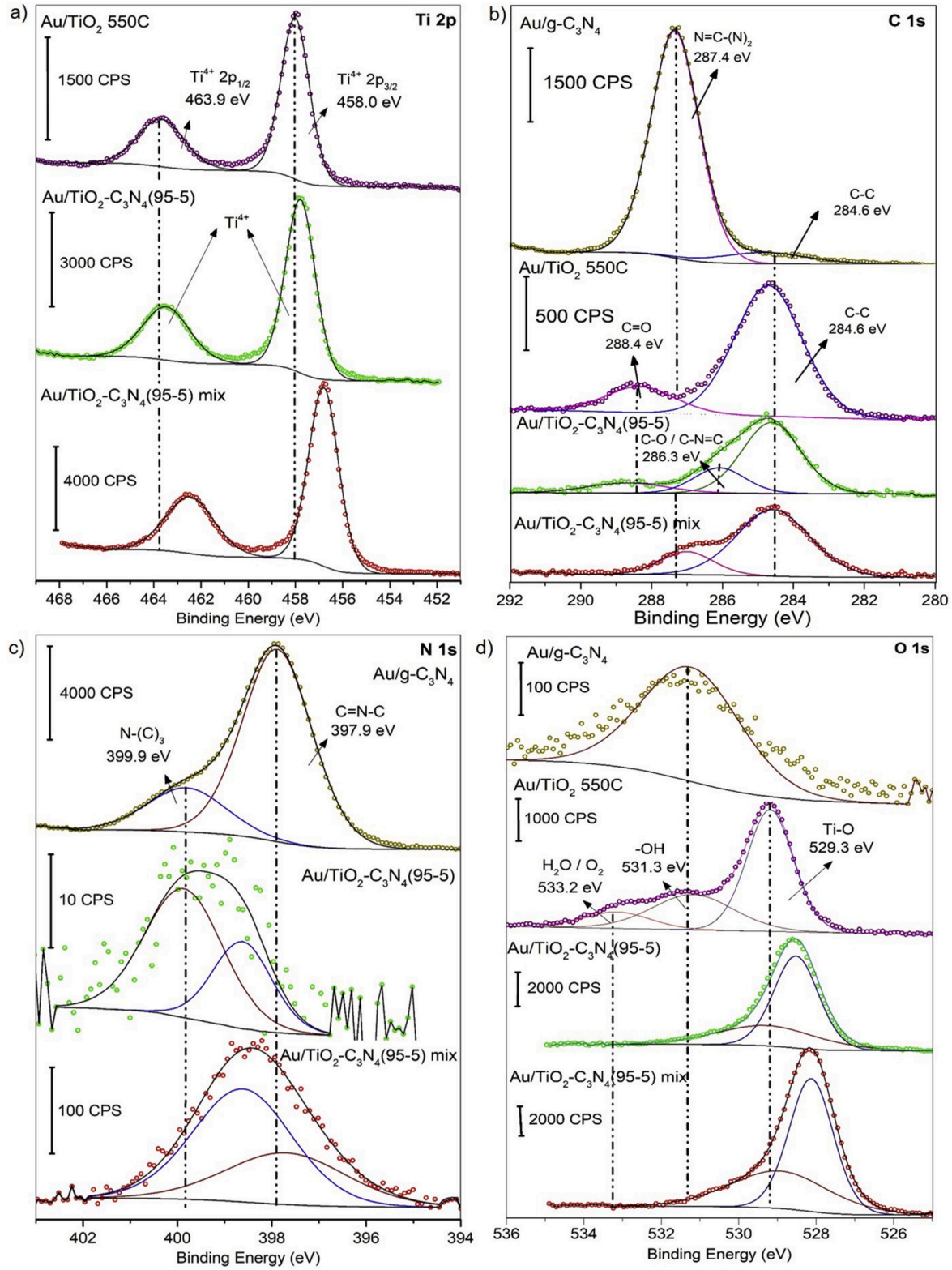

Fig. 2. XPS spectra of the Au/TiO_2-gC_3N_4 (95–5) composite and the references a) Ti 2p spectra, b) C 1s spectra, c) N 1s spectra, and d) O 1s spectra.

Whilst, for the physical mixture shift, also found for Ti 2p and N 1s signals, it confirms the hypothesis described in the Ti 2p section. Globally, the presence of hydroxyl groups in all TiO_2-based samples are of great importance for efficient Au deposition onto the support catalyst. In the case of gC_3N_4-containing materials, one can assume that Au NP deposition may also be achieved as a result of the surface amino groups of gC_3N_4 [37].

The Au 4f signals (Fig. S5b) display the two typical contributions at 86.3 and 82.7 eV ascribed to bulk Au^0 $4f_{7/2}$ and Au^0 $4f_{5/2}$ [38], respectively. With the exception of Au/TiO_2-gC_3N_4 (95–5) physical mixture, a significant shift was found to lower binding energies at 85.3 and 81.5 eV. Thus, this general shift also found for Ti 2p, N 1s, and O 1s signals, confirms the mentioned charge effect in Ti 2p section. In conclusion, this Au 4f doublet has been described in the literature as the interaction of Au NPs with an electron-donor support species [39], namely TiO_2 or gC_3N_4 in our case. Regarding the difference in intensities of Au4f signals is related to the difference in porosity of the samples. XPS is a surface study. Considering the mean free path of electrons, the depth of the catalyst probed by XPS is only a few nm. Hence Au NPs deposited on an essentially non-porous support, such as gC_3N_4 (see Table 1, V_{pore} = 0.05 cm^3/g and Fig. S3), will essentially be located on the outer surface, so that virtually all generated photoelectrons will contribute to the Au4f signal. On the other hand, the same amount of similarly sized Au NPs buried in the porosity of the other samples (Table 1, $V_{pore} > 0.3$ cm^3/g) will yield a much attenuated signal because only a minor amount of emitted photoelectrons will reach the detector, the majority being "trapped" by the walls/particles forming the pores. It is actually common to find attenuated signals for metal catalysts dispersed over porous supports.

3.6. Band edge determination by UV photoelectron spectroscopy

The valence band maximum (VBM) of the TiO_2-gC_3N_4 (95–5) composite and the gC_3N_4 and TiO_2 550C references was deduced from ultraviolet photoelectron spectroscopy (UPS) analysis (Fig. 3a). The TiO_2-gC_3N_4 (95–5) composite exhibited a −5.9 eV VBM, which is located in the middle of the VBM values of the two references (−5.7 eV and −6.1 eV for gC_3N_4 and TiO_2 550C, respectively). However, while positioning the conduction band minimum (CBM), by using the BG obtained by UV–vis, of the three samples the resulting energetic levels are in very similar position. The VBM of the composite is shifted toward positive and negative energy with respect to TiO_2 and gC_3N_4 presumably resulting from the C 2p and N 2p orbitals from the π-conjugated system of gC_3N_4 interacting with Ti^{+4} 2p and O^{2-} 1s orbitals from TiO_2 [40]. In addition, it should be emphasized that the experimental VBM values obtained for both the gC_3N_4 and TiO_2 550C references were similar to the theoretical values reported under vacuum, *ca.* −5.9 and −7.2 eV, respectively [41], which is also the case of UPS measurement.

The UPS and UV–vis results were combined to create a speculative schematic band energy diagram (Fig. 3b) to show the VBM hybrid energy position determined for the TiO_2-gC_3N_4 (95–5) composite.

3.7. TEM and SAED observations

The TEM images (Fig. 4) show two samples: Au/TiO_2 550C (**a, b, c**), and Au/TiO_2-gC_3N_4 (95–5) (**d, e, f**). The two samples exhibit exactly the same Au NP mean particle size (3.4 nm) and associated standard deviation (1.1 nm). This suggests that the small amount of gC_3N_4 (5 wt%) present in Au/TiO_2-gC_3N_4 (95–5) does not impact the Au NPs mean particle size distribution. The other two references samples, Au/TiO_2 and Au/gC_3N_4 exhibit a similar Au NPs mean size (*ca.* 3 nm Fig. S6), suggesting good control of the size and probably good intimate contact with the support. Moreover, the Au NP deposition coverage on the Au/TiO_2-gC_3N_4 (95–5) composite does not greatly change the final Au NP size compared to that of TiO_2 550C, bearing in mind these samples were submitted to the same heating treatment.

All the samples exhibit a monomodal Au particle size distribution, with the exception of the Au/gC_3N_4 reference, which displays rather a quasi-bimodal distribution with small local maxima at 3.5 and 6.5 nm (Fig. S6). The maximum value obtained for the Au/TiO_2-gC_3N_4 (95–5) composite was 2–4 nm, indicating that there is a predominant population of small Au NPs in that range. All samples present the same small standard deviation (1.1 nm), which indicates homogeneous coverage of the NPs over the surface support.

The selected area electron diffraction (SAED) patterns of Au/TiO_2-gC_3N_4 (95–5) are shown in Fig. 5. It can be seen that the distribution varies from element to element and C (red) is the most abundant and well dispersed. The Ti and O atoms exhibit intermediate density, but the

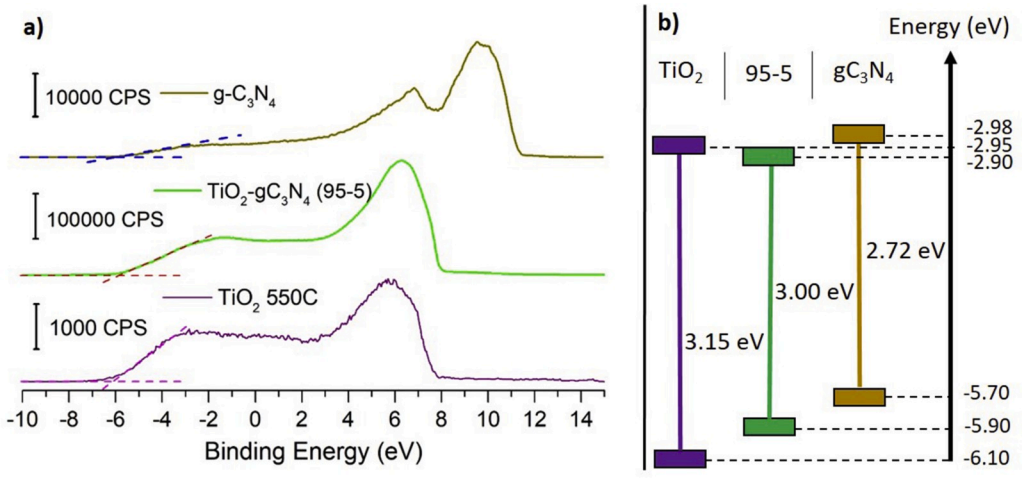

Fig. 3. a) UPS analysis for determination of the VBM of TiO_2-gC_3N_4 (95–5) and the reference materials b) Band energy diagram of the materials.

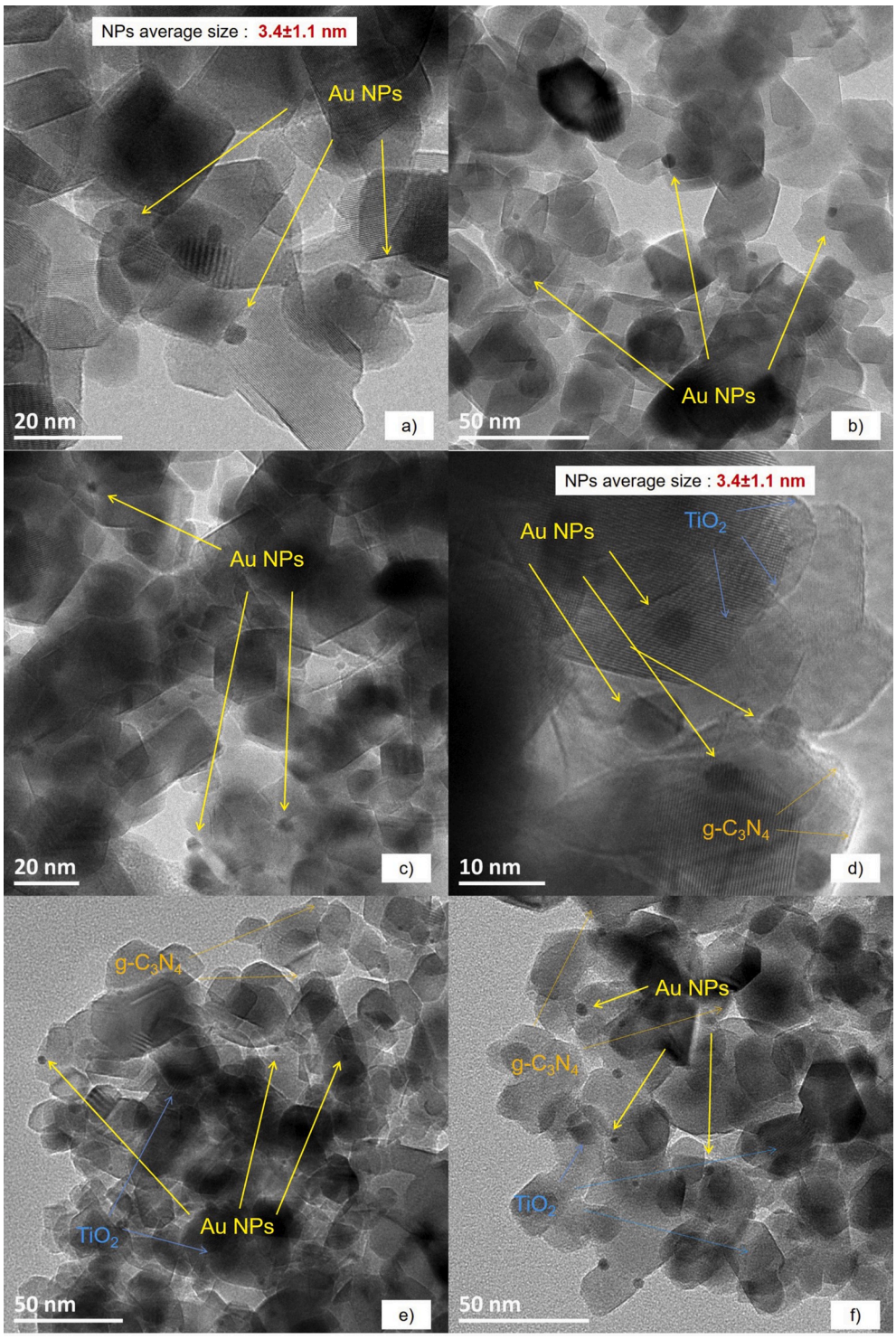

Fig. 4. HRTEM images for the Au/TiO_2 550C reference (a–c) and the Au/TiO_2-gC_3N_4 (95–5) composite (d–f), including the mean particle sizes with their standard deviation.

N atoms show a more attenuated presence in comparison with Ti and O. The least present atom is Au, as expected. Chemical mapping (Fig. S7) in the selected area confirmed the qualitatively presence of the studied elements. Yet, the copper grid used was covered with carbon film inducing impurities and low signals were present, namely for Au, close to the detection limit. For these reasons, appropriate quantification was not thus possible.

3.8. Kinetics of free e−mobility by TRMC

Time-resolved microwave conductivity (TRMC) measurements were performed with 360, 450, 500, and 550 nm laser pulses (Fig. 6a–c and S6) corresponding to the maximum absorption wavelengths of the three components, *i.e.,* TiO_2, gC_3N_4, and plasmon Au, with the exception of 500 nm, which is an intermediate value between the gC_3N_4 visible

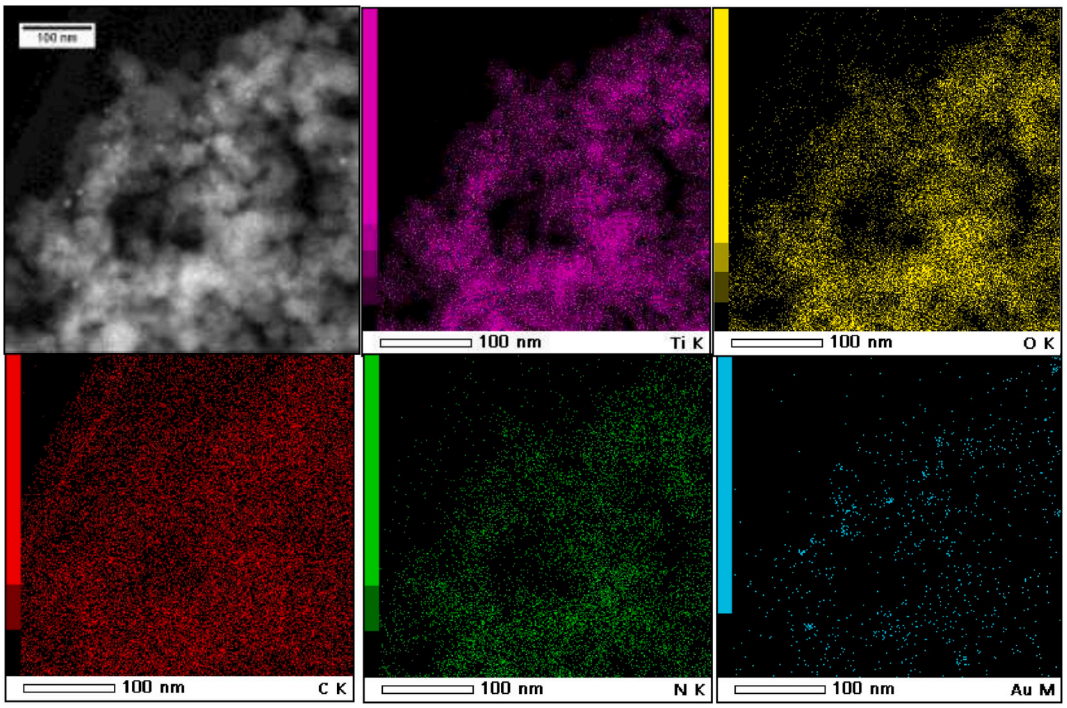

Fig. 5. SAED mapping of 0.3 wt% Au/TiO_2-gC_3N_4 (95–5) composite with localized elements distribution.

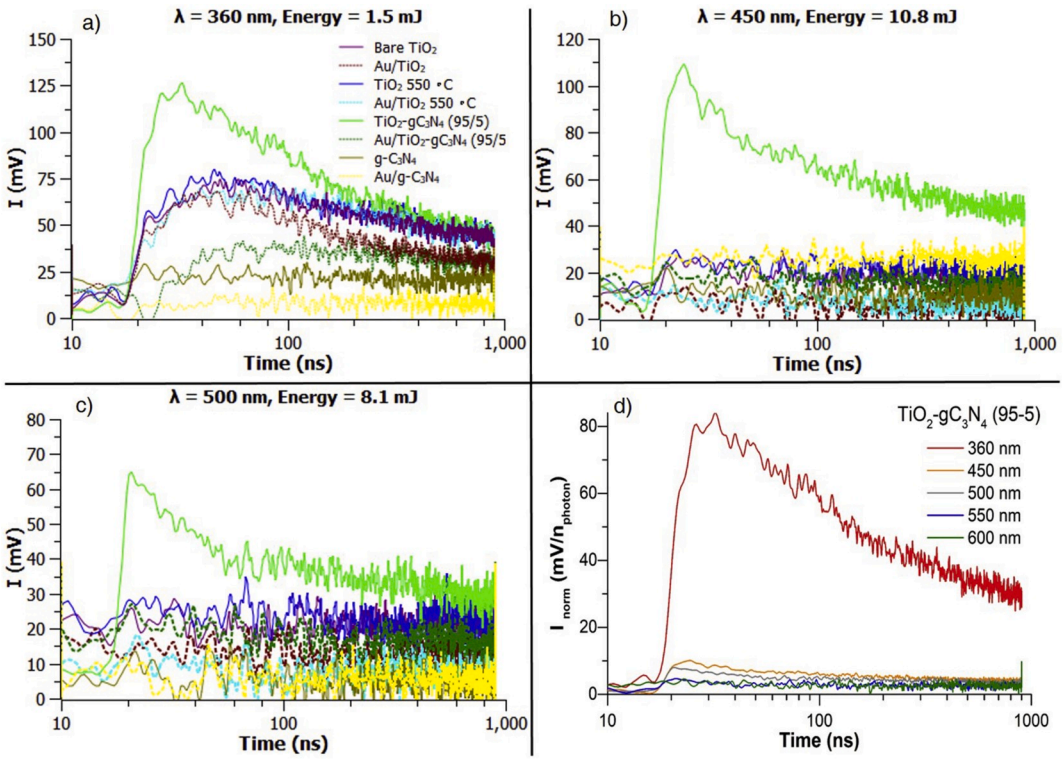

Fig. 6. TRMC signals of Au/TiO_2-gC_3N_4 (95–5) composite compared with TiO_2-gC_3N_4 (95–5), gC_3N_4, TiO_2(P25), TiO_2(P25) 550C, Au/gC_3N_4, Au/TiO_2(P25), and Au/TiO_2(P25) 550C samples at a) 360, b) 450, and c) 500 nm, d) Normalized signals of TiO_2-gC_3N_4 (95–5) composite at 360, 450, 500, 550, and 600 nm.

absorption and the Au plasmonic resonance.

Under UV activation at 360 nm (Fig. 6a), the TiO_2-gC_3N_4 (95–5) composite presents the highest signal of all the samples, which is attributed mainly to the presence of both gC_3N_4 and TiO_2 SCs. Thus, generated free e−mainly come from TiO_2 with an extended assistance of the coupled gC_3N_4. The maximum value of the signal (I_{max}) after the laser pulse excitation reflects the maximum concentration of mobile electrons generated and thus the maximum concentration of dissociated e^-/h^+ pairs created. Higher decay of the signal indicates a higher kinetics of free electron mobility loss either due to increased charges recombination or to electron trapping, thus lowering their mobility. Because the TiO_2-gC_3N_4 (95–5) composite exhibits a more intense signal

than the TiO_2 and gC_3N_4 references, it can be said that photoexcitation promotes a higher amount of the photogenerated e^-/h^+ pairs in the composite than in the references. In addition, the excited electrons located on the gC_3N_4 conductive band (CB) can then be transferred to the TiO_2 CB. This electron flow is consistent with the relative band positions diagram (Fig. 3b) obtained by UPS, where the CB of gC_3N_4 is clearly more positive than the CB for TiO_2. Furthermore, the same behavior was observed for all samples containing Au NPs; they yielded lower signal intensities in comparison with their counterparts without Au NPs, thus providing evidence for the effect of electron traps on the Au NPs. The gC_3N_4 reference did not generate any charge carriers at any of the selected wavelengths excitations, presumably because of the proportion of amorphous phase of the gC_3N_4.

Under visible light activation at 450 nm (Fig. 6b), only the TiO_2-gC_3N_4 (95–5) photocatalyst was able to generate significant charges in comparison with the references. This is the major evidence that gC_3N_4 is actually pumping generated electrons from its more positive CB to the TiO_2 CB, as proposed by UPS, confirming the theory of an effective Z-scheme dynamics system and consequently sensitizing the TiO_2; therefore, the increased spatial separation of charges occurs because of a high quality heterojunction between both SCs.

The signals at 500 nm (Fig. 6c), confirm the photogeneration of charge carriers at 450 nm in the TiO_2-gC_3N_4 (95–5) sample, but in a more attenuated way that at 360 nm excitation, because of the lower absorption capability of gC_3N_4 at that wavelength. Therefore, it can be said that the injection of electrons takes place under the same mechanism previously described in this paper. It can also be seen that there is no further contribution of any of the components of the material at 550 nm (Fig. S8), so one may assume that no significant Au NP SPRs were present.

By comparing this study with a previous similar one [18] dealing with TiO_2(sol-gel)/gC_3N_4 interface with 95/5 relative proportion, as in the present case, different observations can be pointed out. The photosensitization attributed to gC_3N_4 is more pronounced due to its intimate contact with TiO_2 P25 (360–500 nm) rather than TiO_2 sol-gel. In this previous study only photosensitization at 450 nm was observed, thus evidencing that the TiO_2 morphological and structural properties present during the polycondensation step plays a key role by tuning and enhancing the photosensitization effect of gC_3N_4.

The main data provided by TRMC are given by the I_{max} and the immediate decay (I_{40}/I_{max}) is attributed to the decrease in free electrons mobility. The whole decay is not obviously understood because various processes are taking place simultaneously. Nevertheless, $I_{40(ns)}$ can be considered as a reference parameter, because its magnitude may be associated with the relaxation time of trapped holes. The TRMC signals at 360, 450, and 500 nm present different intensities and shapes (without normalization). Thus, I_{40}/I_{max} ratios were calculated for the 360, 450, 500, and 550 nm excitation wavelengths, resulting in values of 0.92, 0.72, 0.74, and 0.49 values, respectively. It can be concluded that the loss of free electrons mobility is highest at the highest I_{40}/I_{max} value, indicating that the TiO_2-gC_3N_4 (95–5) composite recombine from faster to slower in the excitation wavelength order of 360, 450, 500, and 550 nm. These results can also be confirmed by the % percent decay obtained for the mentioned wavelengths, *i.e.* 8, 28, 26, and 51%, respectively.

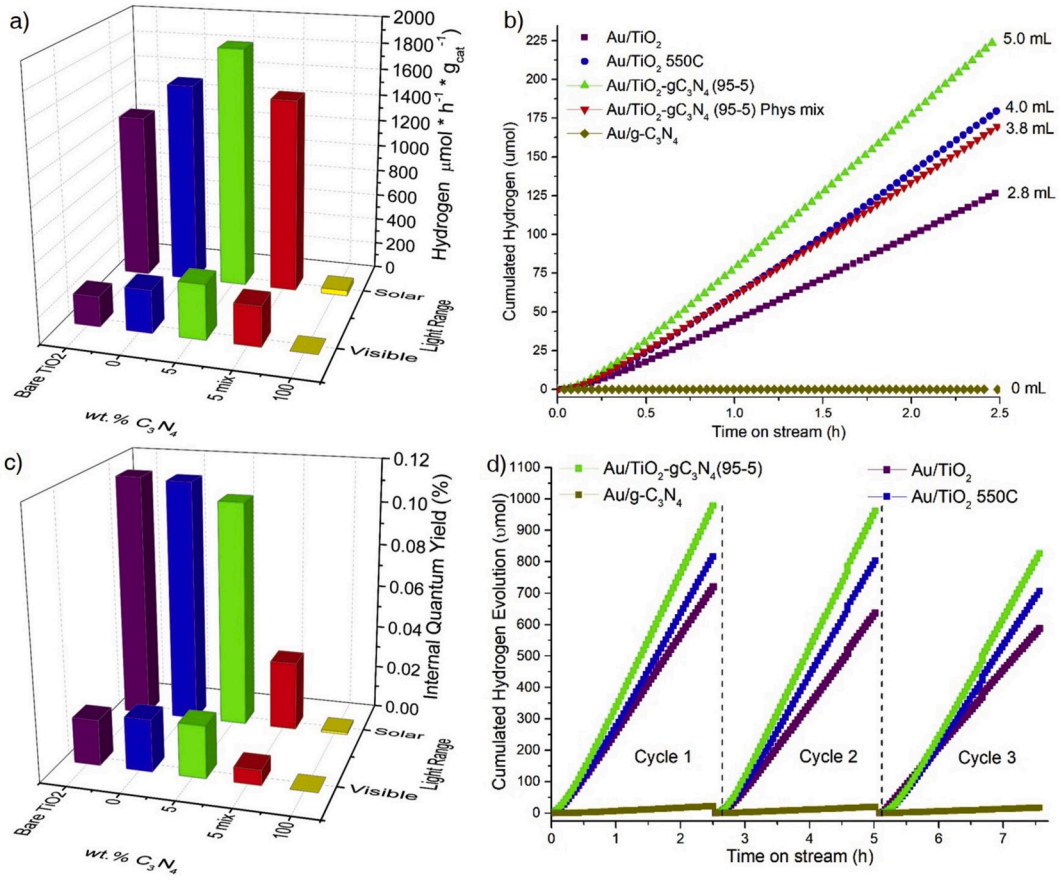

Fig. 7. a) Mean hydrogen formation rate per hour and per mass using 10 mL TEOA (1 vol%) as the sacrificial agent under solar and visible light for the 0.3 wt% Au/TiO_2 references, 0.3 wt% Au/TiO_2/gC_3N_4 composites and the physical mixture photocatalysts b) Cumulative evolution of hydrogen with 1 vol% TEOA under visible-light irradiation c) Internal quantum yield (IQY, %) of the as-prepared photocatalysts under solar and visible light d) Cycling test on the as-prepared photocatalysts with 1 vol% TEOA under solar-light irradiation.

This may suggest that the electron recombination process is less pronounced for TiO_2 than for gC_3N_4. Nevertheless, TiO_2 coupled with gC_3N_4 exhibited an extended generation of charge carriers in the visible region, a moderate recombination rate in the 450–500 nm range, and thus a higher lifetime of charge carriers due to a beneficial spatial charge carriers separation. After normalization of the signals to adjust their different energy pulse densities, comparison of the TiO_2-gC_3N_4 (95–5) photocatalyst at different wavelengths (Fig. 6d) shows a decrease in the signal when exciting at higher wavelengths, which was expected because of the limited light absorption of the composite towards the deep visible range.

3.9. Photocatalytic performance and discussion

When irradiated with artificial solar-light, the Au/TiO_2-gC_3N_4-(95–5) composite has a noticeably superior mean H_2 production rate (1839 μmol h^{-1} g_{cat}^{-1}) over Au/Bare TiO_2(P25), Au/TiO_2 550C, Au/TiO_2-gC_3N_4 (95–5) physical mixture, and Au/gC_3N_4 with differences of 31%, 16%, 27%, and 98%, respectively (Fig. 7a). This suggests a synergic effect between the two SCs at this composition (95−5), presumably sufficient for obtaining either enhanced TiO_2 photosensitization, charge carriers separation, or overall photocatalytic activity in comparison with the closest references, Au/TiO_2 550C and the Au/TiO_2-gC_3N_4-(95–5) physical mixture. In order to emphasize the contribution of Au as co-catalyst, references samples and highest performing composite without Au NPs were evaluated towards H_2 production under solar light irradiation, namely gC_3N_4, TiO_2 550C, TiO_2-gC_3N_4 (95–5) exhibiting 0, 55, and 145 μmol h^{-1} g_{cat}^{-1}, respectively. By comparing these H_2 production rates with their homologs containing 0.3 wt% Au loading, it can be noticed that gC_3N_4 alone is directly dependent of deposited Au NPs to be active, which is in good agreement with literature since this semiconductor is known to present high charge recombination rates [42]. Contrarily, TiO_2 550C and TiO_2-gC_3N_4 (95–5) H_2 production results represent only 4% and 8% of the Au loaded homologs photoactivity. These results paramount the relevance of the plasmonic Au/support Schottky junction, where Au itself plays an important role on boosting the H_2 production, *ca.* > 90% on these type of heterostructure composites.

Regarding, the H_2 production results under visible light showed the same trend as for solar light tests. Increased H_2 production can be seen with the Au/TiO_2-gC_3N_4-(95–5) composite (419 μmol h^{-1} g_{cat}^{-1}) in comparison with Au/Bare TiO_2, Au/TiO_2 550C and the Au/TiO_2-gC_3N_4-(95–5) physical mixture (differences of 45%, 21%, and 27%, respectively). One can see the same trend for the corresponding mean of mass hydrogen formation rate from the cumulative evolution of hydrogen obtained under solar (Fig. S9) and visible-light (Fig. 7b) irradiation. The Au/TiO_2-gC_3N_4 (95–5) sample exhibited the highest cumulated H_2 production with 978 and 224 μmol in only 2.5 h, corresponding to 21.9 mL and 5.0 mL of H_2 formed, respectively. The formation of H_2 under visible light was almost two times higher than that of the reference Au/TiO_2(P25) catalyst.

From the internal quantum yield (IQY) (Fig. 7c) determination, one can see the same trend independently of the irradiation used (solar or visible). However, in this case, there is only a slight difference between the TiO_2 references and the Au/TiO_2(P25)-gC_3N_4 (95–5) composite. Therefore, one can conclude that light absorption (density of absorbed photons) but also efficient charges use is an important parameter contributing to the material's activity. It must be underlined that for the Au/TiO_2(P25)-gC_3N_4 (95–5) physical mixture the IQY is 3.3 times lower than for the composite with the same gC_3N_4 content, underlying the superiority on the light harvesting capacity.

Cycling tests were carried out for the highest performing composite (Au/TiO_2-gC_3N_4 (95–5)) and three references (Au/TiO_2, Au/TiO_2 550C, and Au/gC_3N_4) (Fig. 7d). For each material tested, a decrease in activity was observed. The relative differences for Au/TiO_2-gC_3N_4 (95–5) from the first to the second and third cycles were 2% and 14%, respectively. The relative differences for Au/TiO_2 550C from the first to the second and third cycles were 2% and 12%, respectively. Thus, both samples present relatively good stability on the second cycle, but there is a considerable diminishment for the third cycle that might be attributed to some extent to a possible leaching of Au NPs [43] after the catalysts were filtered and dried, even though at low temperature, before starting the following cycle.

It can be seen from the BET results (Table 1) that the specific surface area of the ternary composites exhibited similar values (*ca.* 50 m^2 g^{-1}), which were similar from that of the TiO_2(P25) reference. However, there is a clear difference in activity between the samples, suggesting that surface area is not a significant influence. In contrast, the BJH results (Fig. S2b) exhibited a significant increase in pore volume of the composite material compared with that of the two reference materials, indicating the drastic changes on the surface textural features bring a synergistic beneficial effect on the activity.

Despite of the absence of change of color, a decrease in the band gap of the composite in comparison with the TiO_2(P25) reference can be seen from UV–vis results (Fig. 1a–b). However, this result suggests some changes in the electronical properties, which are confirmed by the UPS

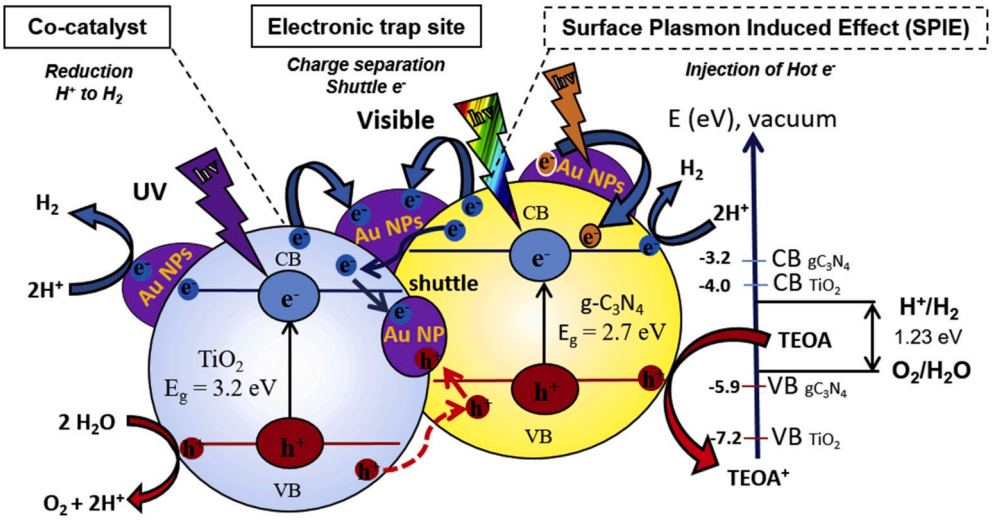

Fig. 8. Charge transfer pathways on 0.3 wt% Au/TiO_2-gC_3N_4 (95–5) ternary composite showing the two possible H_2 reduction paths, H_2O oxidation and TEOA reduction.

results, indicating the formation of new hybrid energy states for the TiO_2-gC_3N_4 (95–5) composite.

The higher lifetime of photogenerated electrons in the TiO_2-gC_3N_4 (95–5) composite, as deduced from TRMC measurements and probably resulting from their trapping onto π-aromatic systems, in combination with the UV–vis and UPS analysis, indicates that the overall improvement of the TiO_2-gC_3N_4 (95–5) composite compared with the references might be related to a synergistic effect from the intimate contact between the TiO_2 and gC_3N_4 SCs. In addition, homogeneously distributed and monomodal Au NPs deposition, also acting as electron traps and probably as a co-catalyst, contribute to the Schottky junction formation of an optimized, well-interfaced, and high quality ternary composite system with enhanced H_2 production properties.

Fig. 8 is an illustrative scheme of the charge transfer process, taking into account all the evidences obtained in this study.

4. Conclusion

A three-step synthetic method was used to design a 0.3 wt% Au/TiO_2(P25)-gC_3N_4 (95–5) ternary composite with a Z-scheme dynamic and optimized interfaces between the three components. This optimized nanocomposite exhibited the highest mass H_2 production rate and cumulated H_2 production compared to references, homolog composites, and mechanical mixture samples. The 0.3 wt% Au/TiO_2(P25)-gC_3N_4 (95–5) composite led to the cumulative formation of 21.9 mL and 5.0 mL of H_2 over 2.5 h under solar and visible-light irradiation, respectively. This activity was much higher than for the Au/TiO_2(P25) reference, which produced 16.1 mL and 2.8 mL under solar and visible-light irradiation, respectively.

Declaration of competing interest

The authors declare that they have no known competing financial interests or personal relationships that could have appeared to influence the work reported in this paper.

CRediT authorship contribution statement

Pablo Jiménez-Calvo: Conceptualization, Validation, Formal analysis, Investigation, Writing - original draft, Writing - review & editing, Visualization, Project administration. **Valérie Caps:** Conceptualization, Methodology, Formal analysis, Writing - review & editing. **Mohamed Nawfal Ghazzal:** Investigation. **Christophe Colbeau-Justin:** Investigation, Formal analysis, Writing - review & editing. **Valérie Keller:** Conceptualization, Methodology, Formal analysis, Resources, Writing - original draft, Writing - review & editing, Supervision, Project administration, Funding acquisition.

Acknowledgements

The authors acknowledge the University of Strasbourg IdEx Program for funding the Ph.D. fellowship of Dr-Ing. Pablo Jiménez-Calvo. In addition, we would like to thank Vasiliki Papaefthimiou for XPS and UPS measurements and discussions (ICPEES, Strasbourg, France), and Dris Ihiawakrim for TEM and SAED measurements (IPCMS, Strasbourg, France).

Appendix A. Supplementary data

Supplementary data to this article can be found online at https://doi.org/10.1016/j.nanoen.2020.104888.

References

[1] M.K. Hubbert, Energy from fossil fuels, Science 109 (1949) 103–109, https://doi.org/10.1126/science.109.2823.103.
[2] REN 21, Global Status Report-Renewables, Paris, 2018. www.ren21.net. (Accessed 27 February 2019).
[3] M. Grätzel, Photoelectrochemical cells, Nature 414 (2001) 338–344, https://doi.org/10.1038/35104607.
[4] D.G. Nocera, The artificial leaf, Acc. Chem. Res. 45 (2012) 767–776, https://doi.org/10.1021/ar2003013.
[5] A. Fujishima, K. Honda, Electrochemical photolysis of water at a semiconductor electrode, Nature 238 (1972) 37–38, https://doi.org/10.1038/238037a0.
[6] P. Nikolaidis, A. Poullikkas, A comparative overview of hydrogen production processes, Renew. Sustain. Energy Rev. 67 (2017) 597–611, https://doi.org/10.1016/J.RSER.2016.09.044.
[7] R. Marschall, Semiconductor composites: strategies for enhancing charge carrier separation to improve photocatalytic activity, Adv. Funct. Mater. 24 (2014) 2421–2440, https://doi.org/10.1002/adfm.201303214.
[8] J. Li, P. Jiménez-Calvo, E. Paineau, M.N. Ghazzal, Metal chalcogenides based heterojunctions and novel nanostructures for photocatalytic hydrogen evolution, Catalysts 1 (2020) 89, https://doi.org/10.3390/catal10010089.
[9] C. Miranda, H. Mansilla, J. Yáñez, S. Obregón, G. Colón, Improved photocatalytic activity of g-C3N4/TiO2 composites prepared by a simple impregnation method, J. Photochem. Photobiol. Chem. 253 (2013) 16–21, https://doi.org/10.1016/j.jphotochem.2012.12.014.
[10] C. Wang, Y. Zhao, H. Xu, Y. Li, Y. Wei, J. Liu, Z. Zhao, Efficient Z-scheme photocatalysts of ultrathin g-C3N4-wrapped Au/TiO2-nanocrystals for enhanced visible-light-driven conversion of CO2 with H2O, Appl. Catal. B Environ. 263 (2020), 118314, https://doi.org/10.1016/j.apcatb.2019.118314.
[11] R. Fiorenza, M. Bellardita, L. D'Urso, G. Compagnini, L. Palmisano, S. Scirè, Au/TiO2-CeO2 catalysts for photocatalytic water splitting and VOCs oxidation reactions, Catalysts 6 (2016) 121, https://doi.org/10.3390/catal6080121.
[12] V. Gombac, L. Sordelli, T. Montini, J.J. Delgado, A. Adamski, G. Adami, M. Cargnello, S. Bernai, P. Fornasiero, CuO x -TiO 2 Photocatalysts for H 2 production from ethanol and glycerol solutions, J. Phys. Chem. 114 (2010) 3916–3925, https://doi.org/10.1021/jp907242q.
[13] M. Song, Y. Wu, G. Zheng, C. Du, Y. Su, Junction of porous g-C3N4 with BiVO4 using Au as electron shuttle for cocatalyst-free robust photocatalytic hydrogen evolution, Appl, Surf. Sci. 498 (2019), 143808, https://doi.org/10.1016/j.apsusc.2019.143808.
[14] M. Altomare, N.T. Nguyen, S. Hejazi, P. Schmuki, A cocatalytic electron-transfer cascade site-selectively placed on TiO $_2$ nanotubes yields enhanced photocatalytic H $_2$ evolution, Adv. Funct. Mater. 28 (2018), 1704259, https://doi.org/10.1002/adfm.201704259.
[15] D. Spanu, S. Recchia, S. Mohajernia, P. Schmuki, M. Altomare, Site-selective Pt dewetting on WO3-coated TiO2 nanotube arrays: an electron transfer cascade-based H2 evolution photocatalyst, Appl. Catal. B Environ. 237 (2018) 198–205, https://doi.org/10.1016/j.apcatb.2018.05.061.
[16] H. Il Kim, J. Kim, W. Kim, W. Choi, Enhanced photocatalytic and photoelectrochemical activity in the ternary hybrid of CdS/TiO2/WO3 through the cascadal electron transfer, J. Phys. Chem. C 115 (2011) 9797–9805, https://doi.org/10.1021/jp1122823.
[17] S. Obregón, G. Colón, Improved H2 production of Pt-TiO2/g-C3N4-MnOx composites by an efficient handling of photogenerated charge pairs, Appl. Catal. B Environ. 144 (2014) 775–782, https://doi.org/10.1016/j.apcatb.2013.07.034.
[18] C. Marchal, T. Cottineau, M.G. Méndez-Medrano, C. Colbeau-Justin, V. Caps, V. Keller, Au/TiO2-gC3N4 nanocomposites for enhanced photocatalytic H2 production from water under visible light irradiation with very low quantities of sacrificial agents, Adv. Energy Mater. 8 (2018), 1702142, https://doi.org/10.1002/aenm.201702142.
[19] F. Vigneron, A. Piquet, W. Baaziz, P. Ronot, A. Boos, I. Janowska, C. Pham-Huu, C. Petit, V. Caps, Hydrophobic gold catalysts: from synthesis on passivated silica to synthesis on few-layer graphene, Catal. Today 235 (2014) 90–97, https://doi.org/10.1016/J.CATTOD.2014.04.016.
[20] P. Kubelka, New contributions to the optics of intensely light-scattering materials Part I, J. Opt. Soc. Am. 38 (1948) 448, https://doi.org/10.1364/JOSA.38.000448.
[21] J. Tauc, Optical properties and electronic structure of amorphous Ge and Si, Mater. Res. Bull. 3 (1968) 37–46, https://doi.org/10.1016/0025-5408(68)90023-8.
[22] S. Brunauer, P.H. Emmett, E. Teller, Adsorption of gases in multimolecular layers, J. Am. Chem. Soc. 60 (1938) 309–319, https://doi.org/10.1021/ja01269a023.
[23] J.H. Scofield, Hartree-Slater subshell photoionization cross-sections at 1254 and 1487 eV, J. Electron. Spectrosc. Relat. Phenom. 8 (1976) 129–137, https://doi.org/10.1016/0368-2048(76)80015-1.
[24] P. Jiménez-Calvo, C. Marchal, T. Cottineau, V. Caps, V. Keller, Influence of gas atmosphere during synthesis of g-C3N4 for enhanced photocatalytic H2 production from water on Aug-C3N4 composites, J. Mater. Chem. A. 7 (2019) 14849–14863, https://doi.org/10.1039/C9TA01734H.
[25] D. Zywitzki, H. Jing, H. Tüysüz, C.K. Chan, High surface area, amorphous titania with reactive Ti $^{3+}$ through a photo-assisted synthesis method for photocatalytic H $_2$ generation, J. Mater. Chem. A. 5 (2017) 10957–10967, https://doi.org/10.1039/C7TA01614J.
[26] J. Zhang, X. Chen, K. Takanabe, K. Maeda, K. Domen, J.D. Epping, X. Fu, M. Antonietti, X. Wang, Synthesis of a carbon nitride structure for visible-light Catalysis by copolymerization, Angew. Chem. Int. Ed. 49 (2010) 441–444, https://doi.org/10.1002/anie.200903886.
[27] C. Marchal, M. Behr, F. Vigneron, V. Caps, V. Keller, Au/TiO2 photocatalysts prepared by solid grinding for artificial solar-light water splitting, New J. Chem. (2016), https://doi.org/10.1039/C5NJ03053F.

[28] B. Hvolbæk, T.V.W. Janssens, B.S. Clausen, H. Falsig, C.H. Christensen, J. K. Nørskov, Catalytic activity of Au nanoparticles, Nano Today 2 (2007) 14–18, https://doi.org/10.1016/S1748-0132(07)70113-5.
[29] P. Judeinstein, C. Sanchez, Hybrid organic-inorganic materials: a land of multidisciplinarity, J. Mater. Chem. 6 (1996) 511–525, https://doi.org/10.1039/JM9960600511.
[30] R. Zhong, Z. Zhang, S. Luo, Z.C. Zhang, L. Huang, M. Gu, Comparison of TiO 2 and g-C 3 N 4 2D/2D nanocomposites from three synthesis protocols for visible-light induced hydrogen evolution, Catal. Sci. Technol. 9 (2019) 75–85, https://doi.org/10.1039/c8cy00965a.
[31] P.V. Zinin, L.-C. Ming, S.K. Sharma, V.N. Khabashesku, X. Liu, S. Hong, S. Endo, T. Acosta, Ultraviolet and near-infrared Raman spectroscopy of graphitic C3N4 phase, Chem. Phys. Lett. 472 (2009) 69–73, https://doi.org/10.1016/j.cplett.2009.02.068.
[32] X. Wei, C. Shao, X. Li, N. Lu, K. Wang, Z. Zhang, Y. Liu, Facile in situ synthesis of plasmonic nanoparticles-decorated g-C $_3$ N $_4$/TiO $_2$ heterojunction nanofibers and comparison study of their photosynergistic effects for efficient photocatalytic H $_2$ evolution, Nanoscale 8 (2016) 11034–11043, https://doi.org/10.1039/C6NR01491G.
[33] Y. Cui, J. Zhang, G. Zhang, J. Huang, P. Liu, M. Antonietti, X. Wang, Synthesis of bulk and nanoporous carbon nitride polymers from ammonium thiocyanate for photocatalytic hydrogen evolution, J. Mater. Chem. 21 (2011) 13032, https://doi.org/10.1039/c1jm11961c.
[34] J.S. Kim, J.W. Oh, S.I. Woo, Improvement of the photocatalytic hydrogen production rate of g-C3N4 following the elimination of defects on the surface, Catal. Today 293–294 (2017) 8–14, https://doi.org/10.1016/J.CATTOD.2016.11.018.
[35] A. Vinu, Two-dimensional hexagonally-ordered mesoporous carbon nitrides with tunable pore diameter, surface area and nitrogen content, Adv. Funct. Mater. 18 (2008) 816–827, https://doi.org/10.1002/adfm.200700783.
[36] T. Bezrodna, G. Puchkovska, V. Shimanovska, I. Chashechnikova, T. Khalyavka, J. Baran, Pyridine-TiO 2 surface interaction as a probe for surface active centers analysis, Appl. Surf. Sci. 214 (2003) 222–231, https://doi.org/10.1016/S0169-4332(03)00346-5.
[37] X. Wang, K. Maeda, A. Thomas, K. Takanabe, G. Xin, J.M. Carlsson, K. Domen, M. Antonietti, A metal-free polymeric photocatalyst for hydrogen production from water under visible light, Nat. Mater. 8 (2009) 76–80, https://doi.org/10.1038/nmat2317.
[38] P. Lignier, M. Comotti, F. Schü, J.-L. Rousset, V. Rie Caps, Effect of the titania morphology on the Au/TiO 2-catalyzed aerobic epoxidation of stilbene, Catal. Today 141 (2009) 355–360, https://doi.org/10.1016/j.cattod.2008.04.032.
[39] V. Caps, S. Arrii, F. Morfin, G. Bergeret, J.-L. Rousset, Structures and associated catalytic properties of well-defined nanoparticles produced by laser vaporisation of alloy rods, Faraday Discuss 138 (2008) 241–256, https://doi.org/10.1039/B706131E.
[40] Z. Lu, L. Zeng, W. Song, Z. Qin, D. Zeng, C. Xie, In situ synthesis of C-TiO2/g-C3N4 heterojunction nanocomposite as highly visible light active photocatalyst originated from effective interfacial charge transfer, Appl. Catal. B Environ. 202 (2017) 489–499, https://doi.org/10.1016/J.APCATB.2016.09.052.
[41] W.-J. Ong, L.-L. Tan, Y.H. Ng, S.-T. Yong, S.-P. Chai, Graphitic carbon nitride (g-C3N4)-based photocatalysts for artificial photosynthesis and environmental remediation: are we a step closer to achieving sustainability? Chem. Rev. 116 (2016) 7159–7329, https://doi.org/10.1021/acs.chemrev.6b00075.
[42] J. Ran, J. Zhang, J. Yu, M. Jaroniec, S.Z. Qiao, Earth-abundant cocatalysts for semiconductor-based photocatalytic water splitting, Chem. Soc. Rev. 43 (2014) 7787–7812, https://doi.org/10.1039/c3cs60425j.
[43] B. Gupta, A.A. Melvin, T. Matthews, S. Dash, A.K. Tyagi, TiO2 modification by gold (Au) for photocatalytic hydrogen (H2) production, Renew. Sustain. Energy Rev. 58 (2016) 1366–1375, https://doi.org/10.1016/j.rser.2015.12.236.

Dr-Ing. Pablo Jiménez-Calvo is a CNRS postdoctoral researcher at the Laboratoire Physique des Solides from the University of Paris Saclay, France. He received his PhD in Materials Chemistry and Physics from the University of Strasbourg, France in 2019, his Master's Degree in Chemical Engineering from the University of Porto, Portugal in 2014, and his Bachelor's Degree in Chemistry at the Universidad Nacional of Costa Rica in 2012. He completed a research internship at the Brussels Innovation Center of Procter & Gamble, Belgium in 2015. His research concerns the design of nanomaterials and chemical reactor engineering both for photocatalytic hydrogen evolution.

Dr. Valérie Caps is a CNRS tenure track research scientist in ICPEES (Strasbourg, France). She received a PhD from the University of Reading (UK) in 2001 under the supervision of S. C.E. Tsang. After two post-doctoral fellowships in Johnson Matthey (Sonning Common, UK) and in the Max Planck Institut für Kohlenforschung (Mülheim an der Ruhr, Germany), she joined CNRS to work in IRCELYON. After a brief period in the KAUST Catalysis Center (Jeddah, Saudi Arabia), she joined the Photocatalysis and Photoconversion team in Strasbourg. Her research interests include the development of chemically grown size- and interface-controlled nanoobjects. She has published over 60 papers.

Dr. Mohamed Nawfal Ghazzal studied Inorganic Chemistry at the Université Claude Bernard, Lyon, France. He received his PhD in 2008 from the Université Paul Verlaine, Metz, France. He moved to Belgium, as postdoctoral fellow at the Université Catholique de Louvain, then as a researcher at Université de Namur and Université de Mons. In France, he obtained a permanent position of Assistant Professor at the Institut de Chimie Physique, Université Paris-Saclay, Orsay. He has published more than 20 research articles in peer-reviewed journals, and 2 patents.

Pr. Christophe Colbeau-Justin studied Inorganic Chemistry at Sorbonne Université, Paris, France. He received his PhD in 1996. He went as a postdoctoral fellowship at Helmholtz-Zentrum Berlin, Germany. He obtained permanent position of Assistant Professor at Université Sorbonne Paris-Nord, Villetaneuse, France. He has been invited researcher at the Universidad Nacional del Litoral, Santa Fe, Argentina. He is currently Full Professor at the Institute of Physical Chemistry, Université Paris-Saclay, Orsay, France. He has published more than 70 research articles in peer-reviewed journals. His research interest concern: photocatalytic nanomaterials and mechanisms (TRMC).

Dr. Valérie Keller received her PhD degree in Chemistry from the University of Strasbourg in 1993 and was appointed in 1996 as researcher at CNRS. She is now senior researcher at ICPEES Institute and responsible of the Team "Photocatalysis and Photoconversion". Her main research activities concern photocatalysis, specifically synthesis of nanomaterials for environmental, energy and health applications. She is the author of over 125 publications in peer-reviewed journals and more than 100 oral communications in international conferences. She is also the author of 16 patents. In 2013 she was awarded the 1st Price of the Strategic Reflection by the French prime Minister.